International Journal of Machine Tools & Manufacture 191 (2023) 104063

Contents lists available at ScienceDirect

International Journal of Machine Tools and Manufacture

journal homepage: www.elsevier.com/locate/ijmactool

Research Paper

Mechanisms of tool-workpiece interaction in ultraprecision diamond turning of single-crystal SiC for curved microstructures

Weihai Huang, Jiwang Yan *

Department of Mechanical Engineering, Faculty of Science and Technology, Keio University, 3-14-1 Hiyoshi, Kohoku-ku, Yokohama, 223-8522, Japan

ARTICLE INFO

Handling editor: Dragos Axinte

Keywords:
Single-crystal silicon carbide
SiC
Diamond turning
Curved microstructured surface
Subsurface damage
Hard and brittle materials

ABSTRACT

Single-crystal silicon carbide (SiC) is one of the most attractive materials for electronics and optics but extremely difficult to cut owing to its hard and brittle properties. While in previous studies, the focus has been placed on machining flat surfaces, in this study, the mechanisms of tool-workpiece interaction in cutting curved microstructures on 4H–SiC (0001) were explored through the ultraprecision diamond turning of micro-dimples. The surface/subsurface of both machined workpieces and used diamond tools were characterized, and the machining characteristics, such as chip formation and cutting forces, were also investigated. It was found that microcracks occurred easily in the feed-in/cut-in area of the dimples, which is caused by a large friction-induced tensile stress due to a large thrust force. The dimples located on the secondary cleavage directions <10−10> (S-dimples) were easy to produce crack-free surfaces, while the dimples located on the primary cleavage directions <−12−10> (P-dimples) were very prone to cause cracks on surfaces, even though the chips were formed in a ductile mode. The dimples located on the in-between direction (I-dimples) were moderately prone to surface cracking. It was also found that although the S-dimple has a crack-free surface, it has the thickest subsurface damage (SSD) layer containing a disordered layer, dislocations, and stacking faults; the SSD layer of the P- and I-dimples do not contain stacking faults; and the SSD layer of the I-dimple is the thinnest. Flank wear with nanoscale grooves on the diamond tool was significant without edge chipping and diamond graphitization detected. By optimizing the cutting conditions, a crack-free micro-dimple array was fabricated with nanometric surface roughness. The findings from this study provide guidance for the manufacture of curved SiC parts with high surface integrity, such as molds for replicating microlens arrays and other freeform surfaces on glass.

1. Introduction

Single-crystal silicon carbide (SiC) is a widely used material in semiconductor and optical applications. Owing to its high hardness and thermal conductivity, as well as low thermal expansion, SiC is also used for manufacturing high-precision molds in glass optics fabrication [1]. However, it is difficult to create a smooth surface on SiC, because of its hardness and brittleness. For manufacturing flat SiC wafers, the conventional method is grinding followed by chemical-mechanical polishing [2–4]. Recently, the demand for fabricating curved microstructures is increasing in the application of integrated optical devices, such as wavefront sensors [5] and imaging systems [6]. Grinding and polishing will not accommodate the needs in such advanced optical systems due to the limitation of the shape flexibility and form accuracy. Although micro milling has been attempted on machining microstructured surfaces on SiC, the machined surface quality and form accuracy need further improvement [7]. As an alternative, single point diamond turning is a promising method for fabricating microstructured surfaces with good surface quality and form accuracy on hard-brittle materials [8,9].

Patten et al. [10] conducted an initial study to demonstrate that the ductile machining of single-crystal SiC can be achieved by diamond turning. After that, several studies have attempted to machine flat surfaces of SiC by diamond turning, but it is found that chipping and flank wear are significant on the tool edge within a short cutting distance [11,12]. Therefore, they failed to produce smooth surfaces with nanometric roughness on SiC. The rapid tool wear due to high hardness (36 ± 2 GPa [13]) impeded the ductile-mode cutting of a larger-size SiC workpiece. Continuous efforts have been made to suppress the tool wear in the diamond cutting of SiC, such as tool-swinging cutting [14], laser-assisted cutting [15], vibration-assisted cutting [16], and applying nanoparticle lubrication [17]. Recently, techniques for enhancing ductile-mode cutting of SiC, including oblique diamond cutting [18] and

* Corresponding author.
E-mail address: yan@mech.keio.ac.jp (J. Yan).

https://doi.org/10.1016/j.ijmachtools.2023.104063
Received 18 May 2023; Received in revised form 23 July 2023; Accepted 28 July 2023
Available online 31 July 2023

surface modification with ion implantation [19,20], have also been proposed. However, to date, there have been no reports of fabricating surfaces with potential applications on SiC by diamond turning. In addition, the superiority of diamond turning of hard-brittle materials, that is, capable of creating microstructured surfaces, is still not demonstrated in SiC machining. On the other hand, some fundamental studies, including taper grooving tests with conventional cutting [21] and vibration-assisted cutting [22], as well as nanoscratching tests [23] were performed to understand the surface/subsurface characteristics in nano cutting of SiC. Molecular dynamics (MD) simulations on 4H–SiC [24], polycrystalline 3C–SiC [25], and 6H–SiC [26,27] were conducted to reveal nano-scale material deformation mechanisms. However, the experiments and simulations in these studies only involved single-pass cutting of SiC without a feed motion perpendicular to the cutting direction. During diamond turning of surfaces, particularly curved microstructured surfaces, the muti-pass cutting induced surface/-subsurface characteristics of SiC remain unclear.

The cutting mechanism of SiC for curved microstructured surfaces is very complicated owing to three-dimensional variations in the tool-workpiece interferential geometry and crystalline anisotropy of the workpiece material. Although there are some literatures that focus on investigating the machining characteristics for fabricating microstructured surfaces on other materials, such as brass [28], nickel [29], and silicon [8,9], none of these materials are as hard and brittle as silicon carbide. How the tool wear affects the machining characteristics of super hard and brittle materials in the ultraprecision cutting of microstructured surfaces is still unknown. According to MD simulations, Goel et al. [30,31] found that the high temperature induced by abrasive action between the SiC workpiece and diamond tool can reduce the hardness of the tool. The graphitization of the diamond tool can occur when cutting SiC, which accelerates the tool wear, but the tool wear caused by tribochemical reactions is not significant. Zhang et al. [14] experimentally investigated the tool wear formation in cutting reaction-bonded SiC with Raman microscopy. Although a non-diamond carbon Raman peak was observed in the worn area of the diamond tool after the machining, the position of this Raman peak does not indicate the formation of graphite, and it is also uncertain whether this non-diamond phase was formed during the cutting process. There is a controversy over whether the microstructural changes of diamond tools have occurred after cutting SiC, because, until now, there have been no reports on direct observation of the subsurface damage of worn diamond tools after machining superhard materials.

In this study, diamond turning of microscale spherical dimples on SiC is explored to clarify two critical issues in the fundamental characteristics of tool-workpiece interaction, namely, workpiece surface/subsurface damages and tool wear. The formation mechanisms of surface and subsurface damages correlated with crystallographic orientation are investigated by observing the morphologies of machined dimples and cutting chips with high-magnification scanning electron microscopy (SEM) and by characterizing the subsurface microstructure of the dimples using cross-sectional transmission electron microscopy (XTEM) and Raman microscopy. The distribution of cutting forces while cutting a dimple is visualized by force mapping with a dynamometer. The tool wear is observed with high-magnification SEM, and the subsurface microstructure of the worn tool is characterized by XTEM. Finally, crack-free micro-dimples are fabricated on SiC with diamond turning. This study provides a deeper understanding of the surface formation and tool wear mechanisms and demonstrates the feasibility of generating microstructured surfaces in the diamond cutting of SiC. The success of this study contributes to manufacturing microstructured optical elements as well as molds for precision glass molding in the optical industry.

2. Materials and methods

A chemomechanically polished single-crystal 4H–SiC (0001) piece with dimension 15 × 10 × 0.35 mm was used as the workpiece. The surface roughness and flatness are 0.2 nm Sa and 0.9 nm, respectively, in a field of 250 × 250 μm^2. It is considered that 4H–SiC is the most difficult-to-cut compared to other types of SiC, such as 3C–SiC and 6H–SiC, but 4H–SiC can produce with the best subsurface integrity [32]. 4H–SiC has a hexagonal close packed lattice structure, as illustrated in Fig. 1a. On the basal plane (0001), the <−12−10> and <10−10> directions are normal to the primary planes {−12−10} and secondary planes {10−10}, respectively. For simplicity, the <−12−10> and <10−10> directions are referred to as the "P" (primary) and "S" (secondary) directions, respectively, and the in-between directions are referred to as the "I" (intermediate) directions, as illustrated in Fig. 1b.

The cutting experiment was carried out on a four-axis (XZBC) control ultraprecision machine tool Nanoform X (AMETEK Precitech Inc., USA) equipped with a slow tool servo (STS) system. The SiC wafer was fixed on the front-end face (diameter 35 mm, thickness 45 mm) of a cylindrical holder (6061 aluminium alloy) by wax. The back-end face of the cylinder (diameter 98 mm, thickness 13 mm) was mounted on the machine spindle using a vacuum chuck. The model number of wax is SHIFTWAX 4202 (NIKKA SEIKO CO., LTD, Japan), which has an adhesive shear strength of 1.9 MPa and a penetration (at 200 g, 60 s) of 1.4 mm. The average thickness of the wax sandwiched between the workpiece and holder was approximately 20 μm, and the deformation of the wax due to the cutting force is less than 0.74 nm. Spherical dimple generation was realised by synchronising the movements of the XZC axes of the machine tool, as shown in Fig. 2a. In each rotation, servo movement of the tool in Z-axis direction was performed to cut workpieces at varying depths, as illustrated Fig. 2b. Meanwhile, the continuous tool feed in X-axis direction generates an envelope curve, as illustrated in Fig. 2c, to form a complete spherical dimple. A single-crystal diamond tool (A.L.M.T. Corp., Japan) was used for cutting. The nose radius (R) of the tool is 1 mm, and the rake angle and relief angle of the tool is 0° and 10°, respectively. The edge radius of the tool was estimated to be less than 50 nm. A piezoelectric dynamometer was applied to collect cutting forces. The sampling frequency for collecting the forces was set to 10 kHz. To acquire cutting chips for observation, the experiments were conducted under dry conditions.

As the basal plane shows 60° symmetry, two dimples were machined at each angular position P, I, and S, and the directions of the tool feed were set to edge-to-centre (E2C) and centre-to-edge (C2E) as illustrated in Fig. 1b. Two kinds of dimples with curvature radius (R_d) of 2 and 3 mm were fabricated. The dimples were located 0.3 mm away from the workpiece rotation centre, and the dimple depth (D) was varied from 0.4 to 1.2 μm. The tool feed rates of 0.25 and 0.2 μm/rev were used under a spindle rotation rate of 30 rpm. The conditions for turning micro spherical dimples on 4H–SiC are summarized in Table 1. After cutting, scanning electron microscopy (SEM), differential interference contrast (DIC) microscopy, white light interferometry, cross-sectional transmission electron microscopy (XTEM), and laser micro-Raman

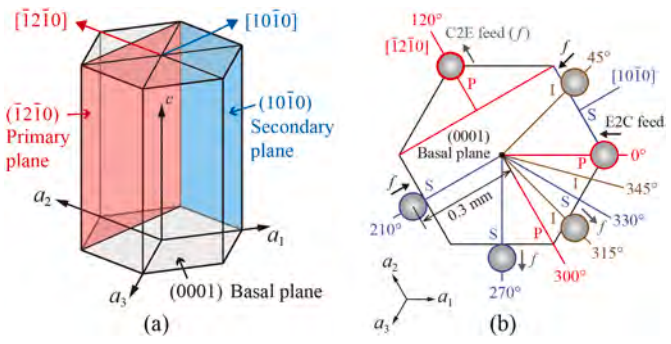

Fig. 1. Schematics of the planar orientation of the machined surface in 4H–SiC crystals: (a) hexagonal close packed lattice structure of 4H–SiC, (b) orientations of the dimples in the basal plane (C2E: centre-to-edge, and E2C: edge-to-centre).

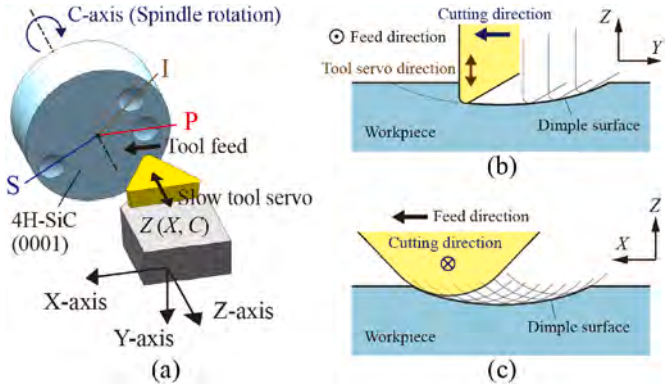

Fig. 2. Schematics of diamond turning spherical dimples with slow tool servo system: (a) configuration of the lathe, (b) a typical curved toolpath along cutting direction, and (c) dimple surface enveloped by multiple toolpaths in tool feed direction.

Table 1
Conditions for turning micro spherical dimples on 4H–SiC.

Parameters	Values
Dimple parameters	
Curvature radius (R_d)	2 and 3 mm
Depth (D)	0.4–1.2 μm
Cutting parameters	
Spindle rotation rate	30 rpm
Tool feed rate (f)	0.25 and 0.2 μm/rev
Depth of cut (d_n)	The same as D
Tool parameters	
Nose radius (R)	1 mm
Edge radius (r)	<50 nm
Rake angle	0°
Relief angle	10°
Cutting atmosphere	Dry

microscopy were used to characterize the morphology and material structural changes of the machined surfaces and cutting chips. XTEM samples were prepared by using a focused ion beam (FIB) system. Before the FIB processing, the workpiece surface was coated with osmium tetroxide (OsO_4) first, followed by the deposition of platinum (Pt).

3. Results

3.1. Surface topography

Fig. 3a presents the DIC microscopy image of the dimples located at the angular position P (P-dimples). For both feed directions C2E and E2C, surface damages tend to occur at the feed-in/cut-in areas of the dimples, as indicated by areas A and B. Fig. 3b and c presents the SEM images of areas A and B. Long parallel cracks are generated perpendicularly to the cutting direction. These cracks are deep and wide, causing partial material to spall off from the substrate, as shown in Fig. 3d. Although the cracks in the two dimples are in different directions, they follow the same family crystallographic directions <−12−10>, indicating that the cracks generated in the P-dimples propagate parallel to the S planes {10−10}. The close-up view of Area C in the dimple with E2C feed (see Fig. 3e) indicates that no cracks form in the cut-out area of the dimple. Instead, evident tool feed marks can be observed on machined surfaces.

Fig. 4a illustrates the DIC microscopy image of the dimples located at the angular position I (I-dimples). Surface damage tends to occur at the location of the feed-in/cut-in areas, as indicated by A and B, which is similar to the damage distribution features in P-dimples. The SEM images of areas A and B (see Fig. 4b and c) indicate that similar to the cracks in P-dimples, the cracks formed perpendicularly to the cutting direction in I-dimples. However, as seen in the close-up view of the cut-in area with E2C feed (see Fig. 4d), numerous short and narrow cracks were generated, which are distinctly different from the cracks formed in the P-dimples.

Fig. 5a illustrates the DIC microscopy image of the dimples located at the angular position S (S-dimples). Unlike the P- and I-dimples, there are no evident damages on the S-dimple surfaces, even at the feed-in/cut-in areas. The SEM observation confirms that, for the shallower dimple (see Fig. 5b), the entire surface is crack-free, while for the deeper dimple, only several microcracks formed in the feed-in/cut-in area, as shown in Fig. 5c. These microcracks are perpendicular to the cutting direction, as displayed in Fig. 5d. However, these cracks are distinctly smaller and fewer compared to the cracks in the P- and I-dimples.

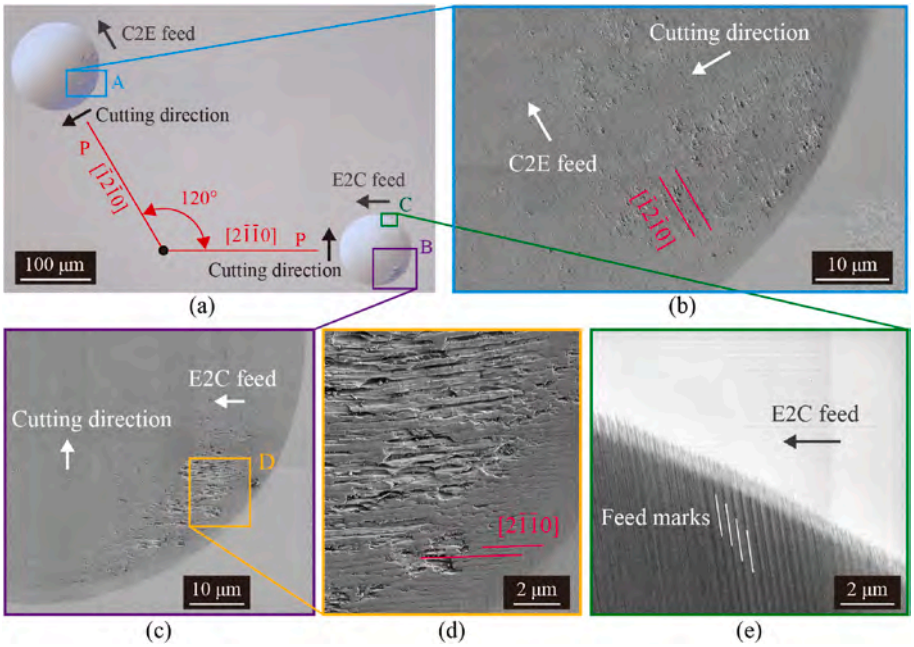

Fig. 3. (a) DIC microscopy image of P-dimples which are located at the angular positions in < −12−10> directions; (b) and (c) are SEM images of the dimples machined under centre-to-edge (C2E) and edge-to-centre (E2C) feeds, respectively, whose observation zones are marked in (a) with blue and purple rectangles, respectively; (d) magnified view of Area D indicated by orange rectangle in (c); (e) SEM image of the cut-out area in the dimple with E2C feed, which marked in (a) with green rectangle. (The red lines marked in (b) and (d) indicate the directions of cracks). (For interpretation of the references to colour in this figure legend, the reader is referred to the Web version of this article.)

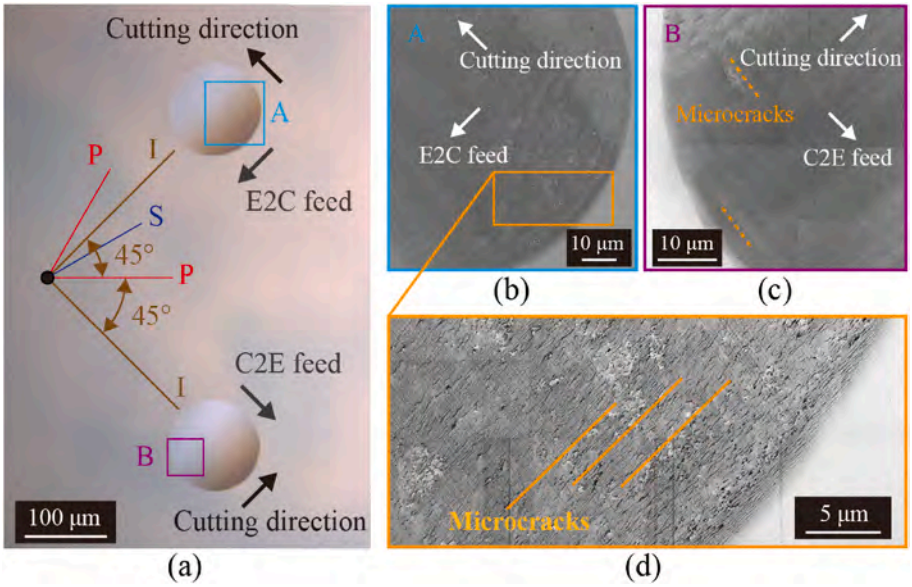

Fig. 4. (a) DIC microscopy image of I-dimples which are located at the angular positions in-between <−12−10> and <10−10> directions; (b) and (c) are SEM images of the dimple machined under edge-to-centre (E2C) and centre-to-edge (C2E) feeds, respectively, whose observation zones are marked in (a) with blue and purple rectangles, respectively; (d) close-up view of the cut-in area in the dimple with E2C feed, which is outlined in (b) with orange rectangle (the orange lines marked in (d) indicate the directions of cracks). (For interpretation of the references to colour in this figure legend, the reader is referred to the Web version of this article.)

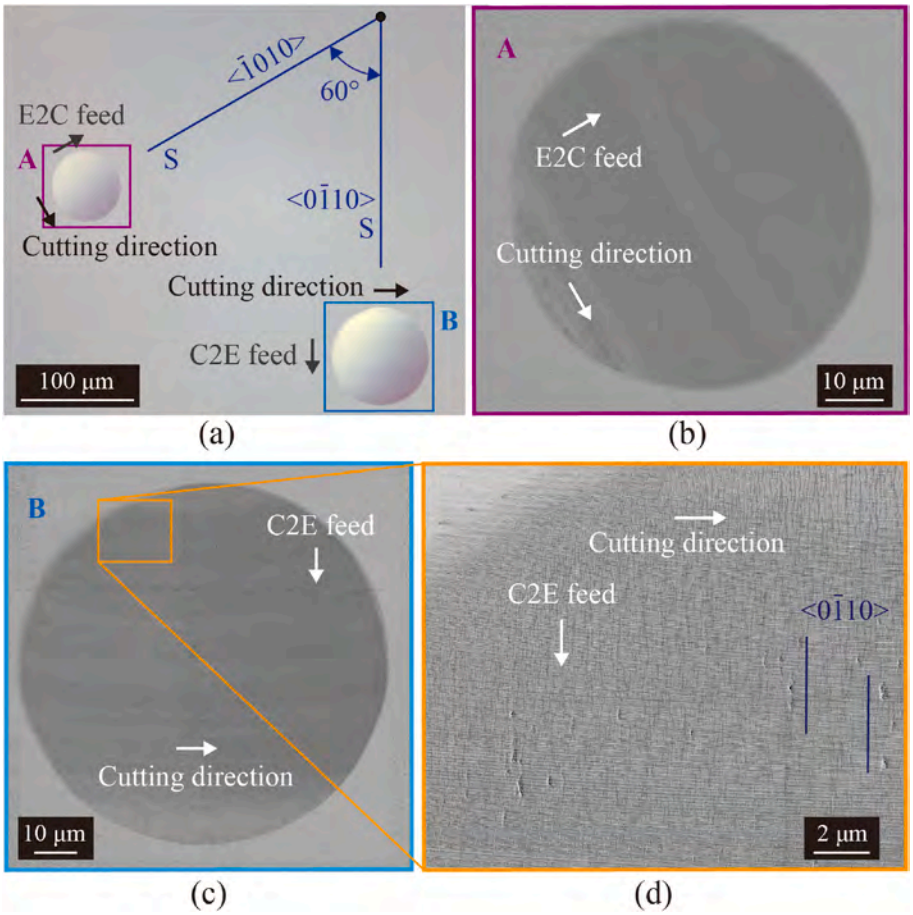

Fig. 5. (a) DIC microscopy image of S-dimples which are located at the angular positions in <10−10> directions; (b) and (c) are SEM images for the dimples machined under edge-to-centre (E2C) and centre-to-edge (C2E) feeds, respectively, whose observation zones are marked in (a) with purple and blue rectangles, respectively; (d) close-up view of the cut-in area in the dimple with C2E feed (The blue lines marked in (d) indicate the directions of cracks). (For interpretation of the references to colour in this figure legend, the reader is referred to the Web version of this article.)

3.2. Chip morphology

Fig. 6a and b shows the SEM images of the chips adhered to the machined surface around the edge and bottom of the P-dimple shown in Fig. 3c, respectively. It can be seen that, although the cracks formed on the surface, generated cutting chips were dominated by the chips resembling curled continuous ribbons. An enlarged SEM image of the area outlined by the red rectangle in Fig. 6a, where the cracks formed, is shown in Fig. 6c. More continuous chips in small sizes are observed. In addition, small particles are observed inside the surface cracks, which may be attributed to the tearing and peeling of the material. Fig. 6d and e presents clear views of the two sides of typical curled continuous chips. The back side has lamella structures, whereas the front side is smooth, which indicates that the chips were generated by plastic deformation

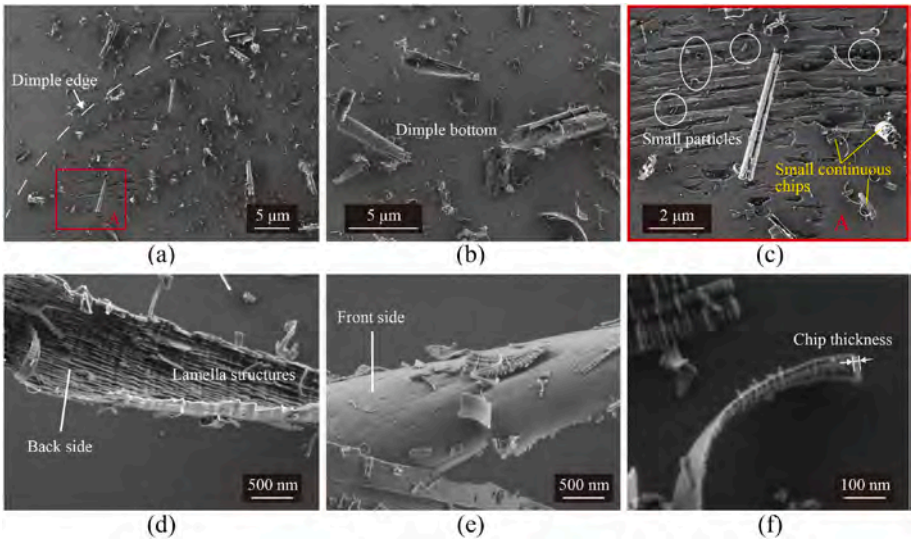

Fig. 6. SEM images of the cutting chips adhered on the P-dimple, which is located at the angular position in [2−1−10] direction: (a) and (d) are general views of the cutting chips around the dimple edge and dimple bottom; (c) enlarged view of Area A outlined in (a) with red rectangle (the white circles marked small particles). Close up images of the (d) back and (e) front side of typical curled continuous chips; (f) high-magnification image for chip thickness measurement. (For interpretation of the references to colour in this figure legend, the reader is referred to the Web version of this article.)

through shearing and/or extrusion similar to that in metal cutting. From the high-magnification SEM image of continuous chips, as exhibited in Fig. 6f, the thickness of the chips is estimated to be ~25 nm. These results indicate that the cutting chips were formed in ductile mode in front of the tool, and they were not affected by the crack formation on the machined surface. The crack formation mechanisms will be discussed in Section 4 in detail. Similarly, the cutting chips on the machined surfaces of I- and S-dimples also presented as curled continuous chips.

3.3. Subsurface damage characterization

To examine the subsurface damage of the machined dimple, cross-sectional TEM observations were performed in the P-, I-, and S-dimples. The TEM sample of each dimple was prepared by FIB milling along the cutting direction at the feed-in/cut-in locations of the dimple where the cracks are easy to form. In addition, to make a comparison, a TEM sample of the pristine surface of 4H–SiC without cutting was made along the same direction as the P-dimple TEM sample as a reference. Fig. 7a presents a general view of the cross section of the pristine workpiece; the subsurface damage layer was too thin to be observed at this magnification. The inset in Fig. 7a is the selected-area diffraction (SAD) pattern of the substrate in the region indicated by the yellow circle. The SAD pattern presents a regular pattern of bright spots, which matches the SAD pattern of 4H–SiC taken in the [2−1−10] zone axis. An enlarged view of the subsurface is shown in Fig. 7b. A very thin damage layer of uneven thickness can be observed. After further enlarging this damage layer, it can be seen from Fig. 7c that this damage layer was divided into two layers: layer 1 next to the surface has a uniform thickness of ~3 nm, while layer 2 beneath layer 1 has a varying thickness. To characterize the microstructures of these two layers, a close-up view of Area D

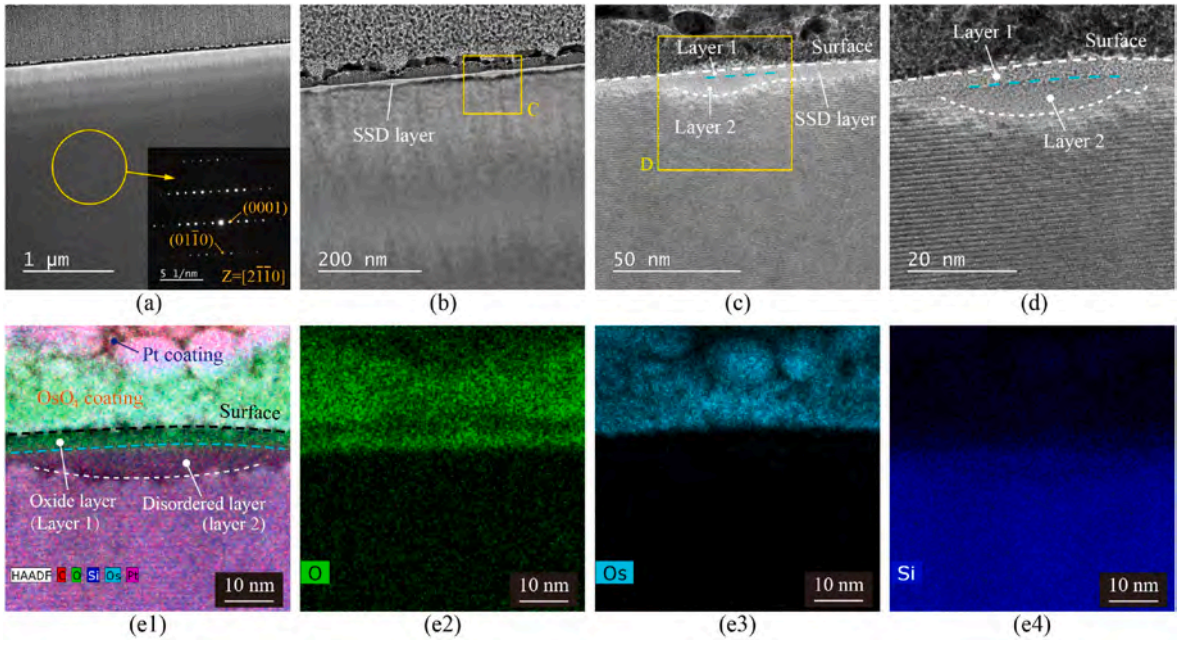

Fig. 7. XTEM observations of the pristine workpiece subsurface: (a) general view of the subsurface (inset is SAD pattern of the area indicated by a yellow circle); (b) enlarged image showing a general view of subsurface damage (SSD) layer, (c) close-up view of the SSD layer indicated by Area C in (b); (d) close-up view of Area D indicated in (c); (e) EDX mapping of selected elements (C, O, Si, Os, and Pt) in the same area shown in (d). (For interpretation of the references to colour in this figure legend, the reader is referred to the Web version of this article.)

indicated in Fig. 7c was taken, as shown in Fig. 7d. It can be seen that in layer 2, heavily disordered lattices were observed; while in layer 1, the lattice structure presented an amorphous-like structure. Energy-dispersive X-ray (EDX) mapping was performed in the same area of Fig. 7d, as depicted in Fig. 7e1–e4. The result shows that layer 1 is silicon oxide, whereas layer 2 is silicon carbide. However, due to the highly disordered structure, the intensity of dispersive X-ray in layer 2 is different from that in the substrate, leading to a slightly different contrast. As no cutting has been done at this moment, the subsurface damage layers should be caused by the chemomechanical polishing during wafer fabrication and/or the sample coating before FIB processing. In particular, layer 1 is caused by the oxidation effect when coating OsO_4 on the workpiece surface, and layer 2 is caused by chemomechanical polishing. As shown in the previous study, OsO_4 is a strong oxidizing agent, causing similar oxidation layers in various materials [33,34].

The TEM image for a general view of the machined subsurface in P-dimple is shown in Fig. 8a. A clear subsurface damage layer with a depth of ~200 nm can be observed below the machined surface, which is much thicker than that in the chemomechanically polished sample (see Fig. 7a). The inset in Fig. 8a presents diffraction spots of the deep region of the substrate, showing the same pattern as the pristine workpiece subsurface, which indicates that no cutting-induced damage has occurred in the deep region of the substrate. An enlarged view of the subsurface damage layer is illustrated in Fig. 8b. As subsurface damage, cracks and dislocations were observed. The cracks tended to spread downward first and then deflect in the cutting direction. This might be the result of the competition of the tensile stresses in the cutting direction induced by the friction of the tool-work interface, and tensile stresses along the shear plane caused by the separation of chips from the substrate as the tool moves forward. The tensile stress in the cutting direction is dominant, causing cracks to spread downward, while due to the lower fracture energy of the basal plane, tensile stresses along the shear plane caused the crack to propagate in the cutting direction. Therefore, it can be inferred that the material spalling observed in Fig. 3d was caused by the intersection between the part of the previous crack that propagated along the cutting direction and the following crack. Moreover, two very thin layers were observed just beneath the machined surface, similar to the pristine workpiece subsurface. To quantify the thickness of the two thin layers, as well as the depth of cracks, a higher magnification of area C in Fig. 8b is presented in Fig. 8c. It can be seen that the thickness of layer 1 is ~5 nm, while layer 2 below layer 1 has a thickness of 5–10 nm. The cracks are initiated from the surface and propagated down through layers 1 and 2 to a depth of ~90 nm from the machined surface. According to the EDX mapping in the same area of Fig. 8c, as depicted in Fig. 8d, it was found that layer 1 was oxidized, while layer 2 was not, which is similar to the subsurface of the pristine workpiece TEM sample. An enlarged image of the two layers is presented in Fig. 8e to clarify their structures further. In layer 2, a mixture of slightly distorted and heavily disordered lattices was observed. In layer 1, the lattice structure became more blurred and disordered, and some regions showed an amorphous-like structure. Since these two layers are too thin to perform selected area diffraction, a high-resolution image was taken to identify the lattice structure in both layers, as shown in Fig. 8f.

Considering that the subsurface damage in the pristine workpiece was removed by the diamond cutting, layers 1 and 2 in the P-dimple TEM sample are newly formed. Layer 1 with partial amorphization has similar features to the oxide layer found in the TEM sample of the pristine surface, both of which are very thin layers with uniform thickness. Thus, it is presumed that diamond cutting caused lattice distortion or polycrystallization of 4H–SiC, which remains as layer 2; while the formation of layer 1 was caused by the oxidation of the top surface by OsO_4 coating in preparing the TEM sample, not by diamond cutting. This is consistent with previous reports on TEM observations of the nanoindentation-induced subsurface deformation region in 4H–SiC, where lattice distortion and nanoscale polycrystallization dominate the subsurface region with no amorphous phase observed [35].

Fig. 8e also shows the starting point of a crack. The lattice to the left of the crack and the lattice to the right of the crack appear misaligned

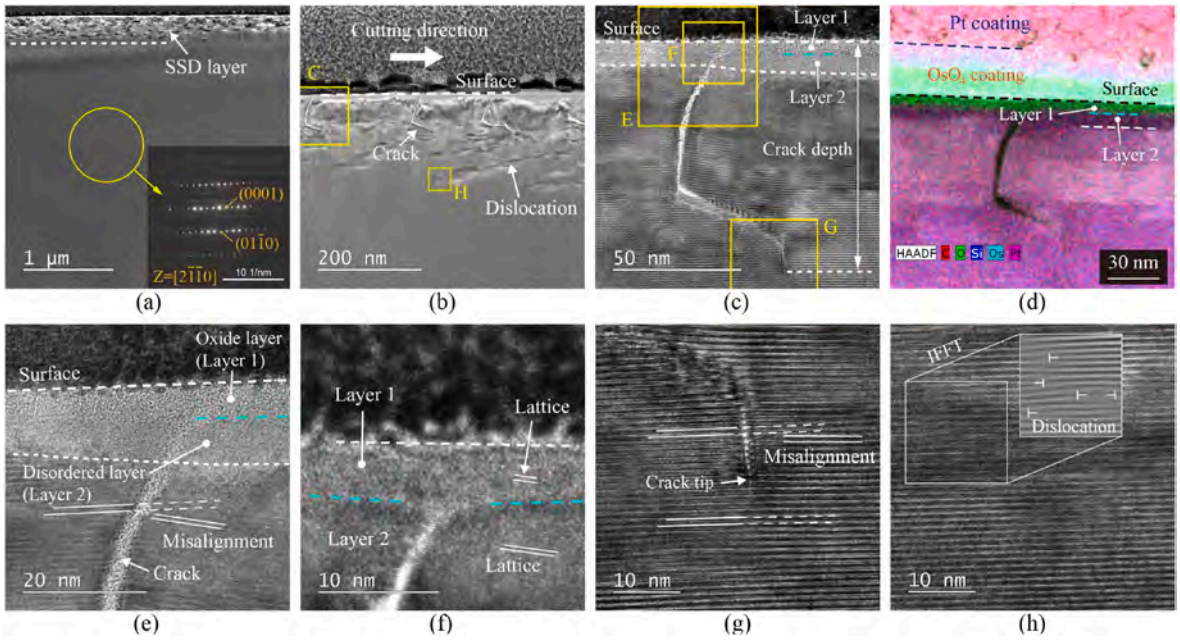

Fig. 8. XTEM observations of the subsurface at the feed-in/cut-in area of the P-dimple which is located at the angular position in [2−1−10] direction: (a) general view of the subsurface damage (SSD) layer (inset is SAD pattern of the area indicated by a yellow circle); (b) enlarged image showing subsurface damage, (c) close-up view of the crack indicated by Area C in (b); (d) EDX mapping of selected elements (C, O, Si, Os, and Pt) in the same area shown in (c); (e) close-up view of Area E indicated in (c); (f) high-resolution image of Area F indicated in (c); (g) high-resolution image of the crack tip indicated by Area G in (c); and (h) high-resolution image of Area H outlined in (b) (inset is inverse fast Fourier transform (IFFT) result showing dislocation). (For interpretation of the references to colour in this figure legend, the reader is referred to the Web version of this article.)

with a large angle; in particular, the left side is deflected downwards relative to the right side. This implies that when the tool cut into the workpiece to create a dimple, the downward force caused lattice deformation, consequently leading to surface cracking owing to the low fracture toughness of the workpiece material. Fig. 8g illustrates a high-resolution image of the crack tip. The misalignment angle of the lattice to the left and right of the crack tip becomes smaller compared to the starting point of a crack, while at the location below the crack tip, no significant misalignment has occurred. This result confirms that the lattice deformation is the cause of cracking. Fig. 8h illustrates a high-resolution image of the region with dark lines indicated by H in Fig. 8b. Dislocations are present in this area, as demonstrated in the inset, which depicts an inverse fast Fourier transform (IFFT) result. In 4H–SiC, dislocations are classified into threading dislocations and basal plane dislocations. However, during cutting, basal plane dislocations with a Burgers vector of 1/3 <11−20> tend to form instead of threading dislocations, because shear stresses dominate the stress field [36]. In addition, a basal plane dislocation is prone to dissociate into two partial dislocations, 1/3 <10−10> and 1/3 <01−10> [37].

The TEM image for a general view of the machined subsurface in I-dimple is shown in Fig. 9a. A subsurface damage layer with a depth of ~60 nm can be observed in the near machined surface. The subsurface damage layer in the I-dimple is much thinner than that in the P-dimple. The inset in Fig. 9a presents diffraction spots below the subsurface damage layer, showing a pattern that differs from P-dimple due to the different zone-axis. These clear diffraction spots indicate that the subsurface in a deeper location of the sample is free of damage. An enlarged view of the subsurface damage layer is illustrated in Fig. 9b. The main forms of subsurface damage are the same as those in P-dimple, including cracks, dislocations, and two thin layers (layers 1 and 2) with different microstructures from the substrate. The cracks are still featured by deflection in the cutting direction. However, compared with the P-dimple, in the I-dimple the depth of cracks is smaller, and the two layers are thicker, especially layer 2. It can be seen from Fig. 9c that the depth of the crack is ~47 nm from the machined surface. Layer 1 has a uniform thickness of ~6 nm, and layer 2 has a thickness ranging from 10 to 13 nm. The EDX mapping results, as depicted in Fig. 9d, again confirmed that layer 1 was an oxide layer. To characterize the microstructure of the two layers, an enlarged view of the two layers is illustrated in Fig. 9e. Compared with layer 2 in the P-dimple, the ordered lattices in layer 2 in the I-dimple became less noticeable, indicating that the subsurface material underwent a more severe distortion in the cutting process. This may be due to fewer and shallower cracks forming, which provided higher stress in the subsurface. In layer 1 of the I-dimple, the majority of the region was featured by an amorphous-like structure. The high-magnification image of the two layers, as shown in Fig. 9f, further confirmed the dominance of the amorphous-like and highly disordered structures in layers 1 and 2.

On the other hand, like the presence of misalignment in the P-dimple, the lattices of the two sides of the crack appear misaligned as well in the I-dimple, but with a smaller misaligned angle. Fig. 9g shows a high-resolution image of the crack tip. The misalignment angle of the lattice becomes smaller as the crack propagates into a deeper location. The misalignment in I-dimple disappeared at a shallower depth than P-dimple; thus, the crack depth in the I-dimple is shorter than that in the P-dimple. Fig. 9h illustrates a high-resolution image of the region with a dark area indicated by H in Fig. 9b. The inverse fast Fourier transform (IFFT) result indicates that dislocations are present below the disordered layer.

The TEM image for a general view of the machined subsurface in S-dimple is shown in Fig. 10a. A subsurface damage layer with a depth of ~220 nm can be observed in the near machined surface. The subsurface damage layer in the S-dimple is a little thicker than in the P-dimple. The diffraction spots below the subsurface damage layer are clear, as shown in the inset of Fig. 10a, and their pattern is the same as the SAD pattern taken in the [−101−2] zone axis. An enlarged view of the subsurface damage layer is illustrated in Fig. 10b. Although the subsurface damage layer of the S-dimple is the thickest compared to that of P- and I-dimples, no cracks were generated in the material. Instead, stacking faults appear as a form of subsurface damage, together with dislocations and two thin

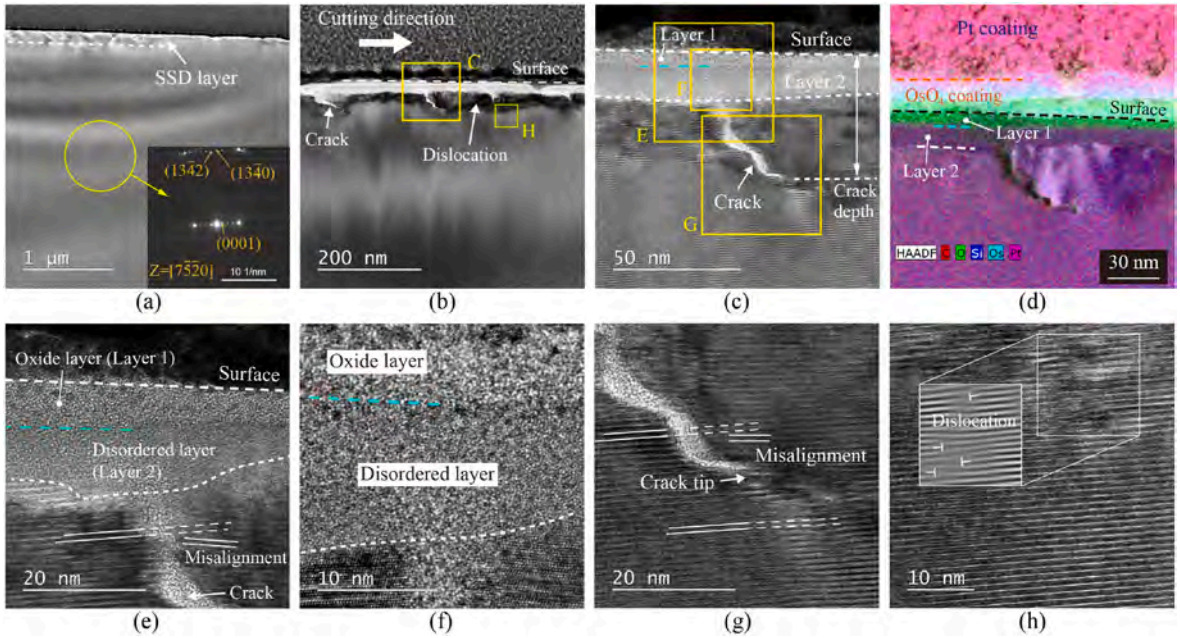

Fig. 9. XTEM observations of the subsurface at the feed-in/cut-in area of the I-dimple which is located at the angular position in-between [11−20] and [10−10] directions: (a) general view of the subsurface damage (SSD) layer (inset is SAD pattern of the area indicated by a yellow circle); (b) enlarged image showing subsurface damage, (c) close-up view of the crack indicated by Area C in (b); (d) EDX mapping of selected elements (C, O, Si, Os, and Pt) in the same area shown in (c); (e) close-up view of Area E indicated in (c); (f) high-magnification image of Area F indicated in (c); (g) high-resolution image of the crack tip indicated by Area G in (c); and (h) high-resolution image of Area H outlined in (b) (inset is inverse fast Fourier transform (IFFT) result showing dislocation). (For interpretation of the references to colour in this figure legend, the reader is referred to the Web version of this article.)

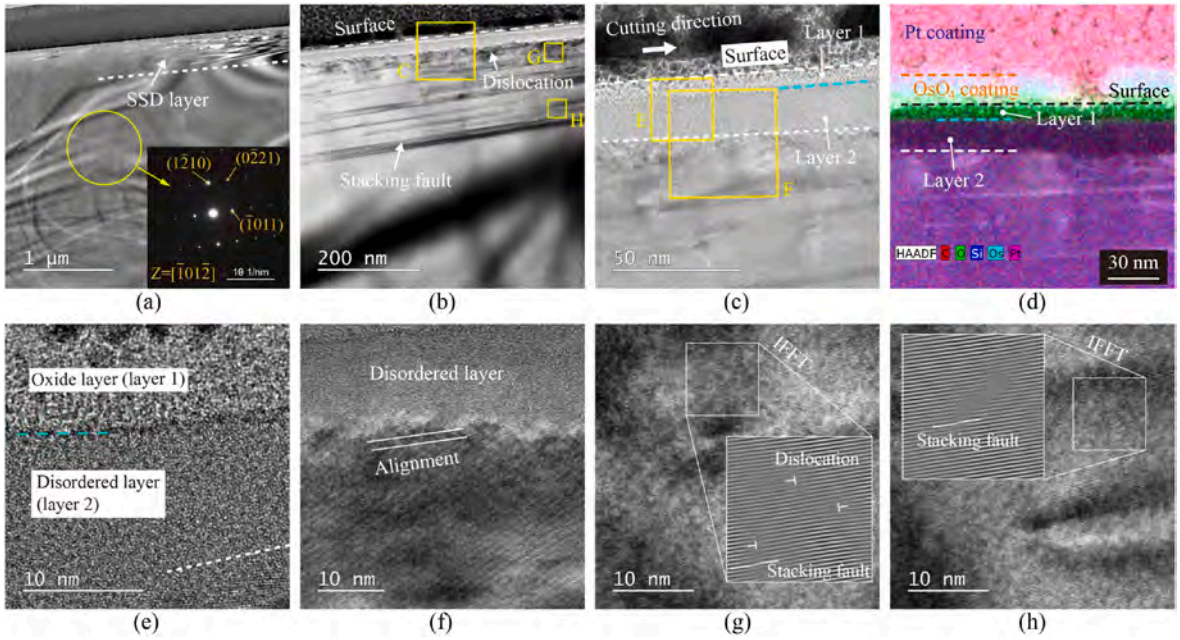

Fig. 10. XTEM observations of the subsurface at the feed-in/cut-in area of the S-dimple which is located at the angular position in [10−10] direction: (a) general view of the subsurface damage (SSD) layer (inset is SAD pattern of the area indicated by a yellow circle); (b) enlarged image showing subsurface damage; (c) close-up view of the near-surface indicated by Area C in (b); (d) EDX mapping of selected elements (C, O, Si, Os, and Pt) in the same area shown in (c); (e) close-up view of Area E indicated in (c); (f) close-up view of Area F indicated in (c); (g) high-resolution image of Area G outlined in (b) (inset is inverse fast Fourier transform (IFFT) result showing dislocation and stacking fault); and (h) high-resolution image of Area H outlined in (b) (inset is IFFT result showing stacking fault). (For interpretation of the references to colour in this figure legend, the reader is referred to the Web version of this article.)

layers, i.e., the oxide layer and the disordered layer. The stacking faults extend deeply into the machined subsurface, even deeper than the cracks and dislocations formed in P- and I-dimples. A close-up image of the oxide layer and disordered layer is illustrated in Fig. 10c, and its EDX mapping results are depicted in Fig. 10d. Compared with P- and I-dimples, S-dimple has the thickest disordered layer with a thickness ranging from 18 to 22 nm, while its coating-induced oxide layer has a thickness of ~6 nm, similar to those in P- and I-dimples. Fig. 10e shows a high-magnification view of the microstructure of the two layers. Since no cracks were formed, the subsurface underwent a more severe plastic deformation; as a result, few lattices can be found in these two layers. Fig. 10f shows an enlarged view of the boundary of layer 2 and the bulk region. In contrast, clear regular lattices can be observed just beneath the disordered layer without the lattice misalignment like in the TEM samples of P- and I-dimples; thus, no cracks formed in the material. High-resolution images of the regions nearer and further from the disordered layer, indicated by G and H in Fig. 10b, respectively, are presented in Fig. 10g and h. The inset of Fig. 10g indicates that dislocations and stacking faults were generated near the machined surface, and the inset of Fig. 10h indicates that stacking fault is the major form of subsurface damage away from the machined surface.

The Raman spectra of the machined surfaces and cutting chips were also measured and compared with the unmachined workpiece, as depicted in Fig. 11a. The unmachined surface presents a typical spectrum of 4H–SiC, featured by folded transverse acoustic (FTA), folded transverse optical (FTO), and folded longitudinal optical (FLO) peaks at 203, 777, and 977 cm^{-1}, respectively [38]. The machined surfaces and cutting chips exhibit almost the same spectra as the unmachined surface, which is consistent with the TEM observation results that no amorphous layer exists in the machined subsurface. Fig. 11b presents the mapping result of the FTO peak shift around an S-dimple. The feed-in/cut-in area indicates a lower Raman shift (darker region), which suggests a higher tensile residual stress in this area.

3.4. Cutting forces

During the cutting of a S-dimple with C2E feed, the principal force (F_c) and thrust force (F_t), were measured when the tool feeds along the

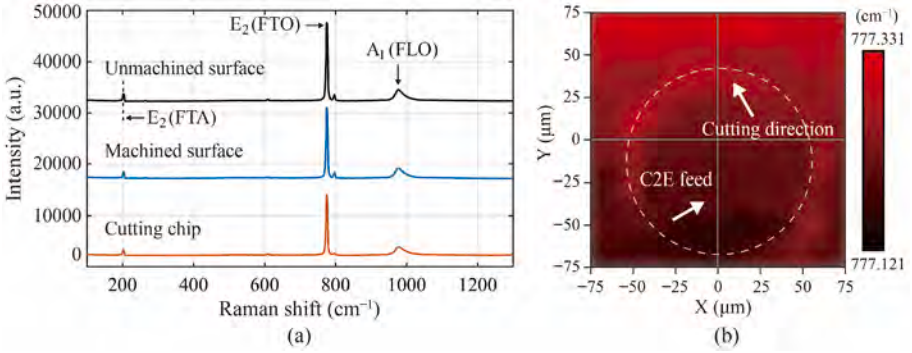

Fig. 11. (a) Raman spectra of cutting chips as well as unmachined and machined surfaces. (b) Raman mapping of E_2(FTO) peak shifts around an S-dimple which is located at the angular position in [10−10] direction (the dashed white line marks the edge of the dimple).

X-axis. The cutting forces in one workpiece rotation were collected for every 5 μm of tool feed in the X-axis. Fig. 12a and b shows the mapping of F_c and F_t based on the collected forces data. The shape of the cutting forces distribution is not a circle; in particular, the length in the cutting direction is long, and the length in the feed direction is short, because in the cutting of a spherical dimple, the tool nose radius compensation has been considered in the toolpath planning to reduce the form error caused by the tool nose radius [39]. To confirm this, a three-dimensional topography of relative toolpaths to the workpiece for generating a spherical dimple is schematically illustrated in Fig. 12c. The shape of the tool path for cutting a dimple is similar to that of the cutting forces distribution, and the variation trend of the depth of cut is consistent with the trend in cutting forces. To quantify the direction of the resultant force during cutting the dimple, a force angle β is defined as the angle between the resultant force and F_c, and its variation is plotted in Fig. 12d. It can be seen that the largest force angle, indicating thrust force is dominant, is observed at the location of the feed-in/cut-in area, which corresponds to the area where cracks tend to form. This implies that the thrust force has a significant role in crack formation. In addition, for each circle of toolpath in the cutting direction, β gradually decreases when the tool advances from the cut-in to the cut-out side. To more clearly analyse the forces distribution along the feed direction, the peak force components at various X positions are plotted in Fig. 12e. The forces are asymmetrically distributed along the X-axis. In particular, they start increasing rapidly at the beginning of the tool feed-in and then decrease before the tool feeds to the dimple centre. The forces continue to decrease while the tool feeds out. In the early feed-in stages, F_c is greater than F_t, but when both forces reach their maximums, F_c becomes less than F_t until the tool feeds out of the dimple. The features of the cutting forces are related to the variation in the undeformed chip thickness, which will be discussed in Section 4. On the other hand, to analyse the forces distribution along the cutting direction, the real-time changes in F_c and F_t at $X = 0.275$ mm are plotted in Fig. 12f. The trends of variation in F_c and F_t are consistent with that of the dimple depth. However, there is a shift between the peaks of F_c and F_t, that is, the F_c peak appears later than the F_t peak. The real-time changes in force angle at $X = 0.275$ mm are also plotted in Fig. 12f, which clearly shows a gradual decrease in force angle from cut-in to cut-out in one circle of the toolpath.

3.5. Tool wear

Fig. 13a and b presents the SEM images of the cutting edge of the diamond tool before and after cutting four dimples. After cutting four dimples, a uniform flank wear land was formed without any occurrence of edge chipping, which may be attributed to the very small undeformed chip thickness during cutting. In addition, numerous nanoscale grooves with an orientation in line with the cutting direction were generated in the flank wear land. This might be because SiC is a superhard material; meanwhile, the marks caused by continuous tool feeding on the machined surface are constantly rubbing against the tool flank face during cutting. In other words, the formation of nanoscale grooves on the tool flank face may be a result of continuous squeezing of the wear land by the tool feed marks on the machined surface [14].

To examine the possible subsurface microstructural changes in the diamond tool caused by cutting SiC, cross-sectional TEM observations of the diamond tool were performed. The TEM sample of the tool was made in a plane normal to the cutting edge by FIB milling, as show in Fig. 13c. Fig. 14a shows a general view of the tip of the worn tool. The tool parameters listed in Table 1, that is, the tool has 0° rake angle and 10° relief angle, can be directly seen from this cross-section sample. Fig. 14b presents an enlarged image of the wear land on the tool flank face. The flank wear land is normal to the rake face, which implies that the tool wear started from the tip of the fresh tool and increased uniformly, layer by layer in the direction parallel to the cutting direction, towards the back end of the tool. Different from the machined subsurface of SiC that exhibited various defects, no obvious subsurface damage was observed in the diamond tool. A high-resolution image of the tool tip is present in Fig. 14c. No apparent layer with a microstructure different from the substrate was found, although previous studies by MD simulations

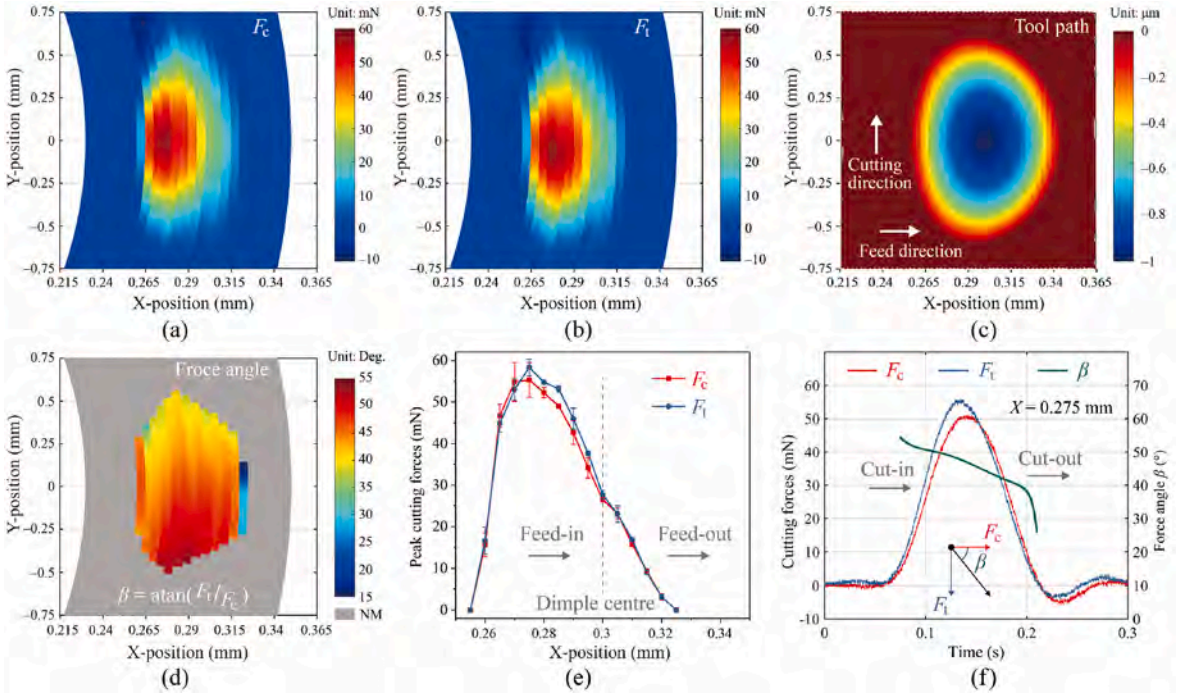

Fig. 12. Mapping of cutting forces: (a) principal force F_c and (b) thrust force F_t in cutting a S-dimple, which is located at the angular position in [10−10] direction, with centre-to-edge feed; (c) three-dimensional topography of relative toolpath to the workpiece after tool nose radius compensation; (d) distribution of force angle β in cutting the S-dimple; (e) changes of peak force components with respect to the X position; (f) real-time plots of force components and force angle in one cycle of toolpath when the tool is fed to $X = 0.275$ mm.

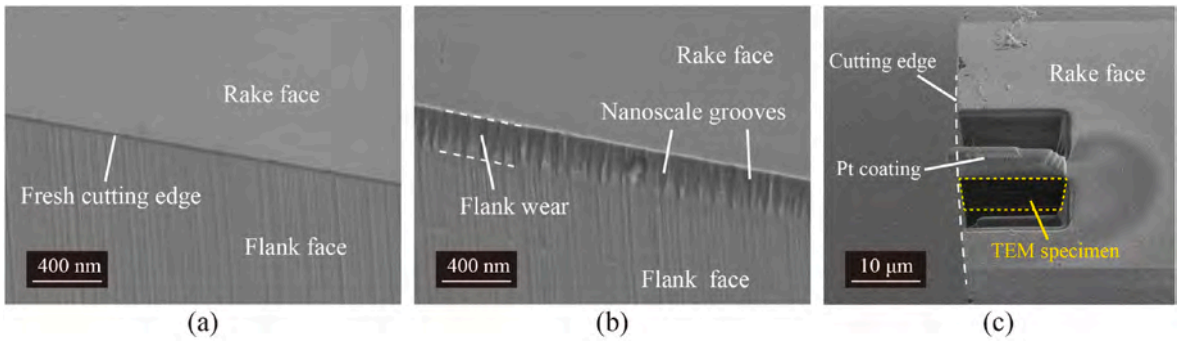

Fig. 13. SEM images of the cutting edge of the tool: (a) before, and (b) after machining four dimples; (c) after the focused ion beam milling for preparing TEM specimen.

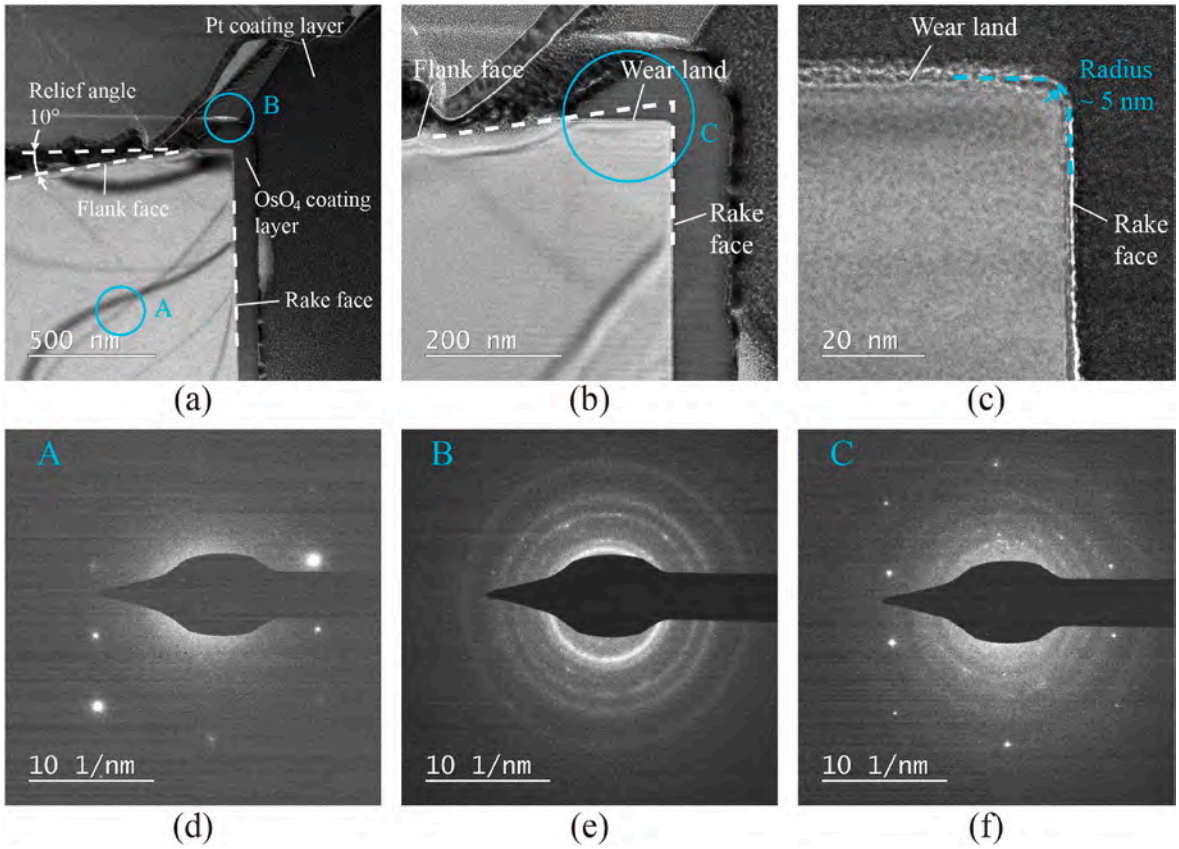

Fig. 14. XTEM observations of the subsurface of the worn tool: (a) general view of the tool tip; (b) enlarged image of the wear land; (c) high-resolution image of the tool tip; (d)–(f) are selected area diffraction (SAD) patterns of areas A, B, and C indicated by blue circles in (a) and (b).

reported that graphitization of the diamond tool would be occurred after cutting SiC [30,31]. To further investigate the phase transformation of the tool after cutting SiC, the selected area diffraction was performed in the worn tool. Since the smallest selected area aperture for diffraction patterns is about 200 nm in diameter due to the limitation of the equipment, it is difficult to characterize the diffraction pattern of the near-surface of the wear land only. Therefore, diffraction patterns from three regions were collected, including the tool substrate, coating layers, and interface between the tool and coating, as indicated by blue circles A, B, and C in Fig. 14a and b. Thus, the graphitization of the wear land can be figured out by comparing the patterns of region A with the subtraction of the pattern of region B from that of region C. The clear diffraction spots of the tool substrate shown in Fig. 14d indicate that the pristine tool material is a single crystal. While in the coating layers, ring diffraction patterns, and diffraction spots that are different from the diamond diffraction spots were observed, as shown in Fig. 14e. The ring pattern was caused by the amorphous phase of the Pt coating layer, and the spot pattern was due to the OsO_4 coating layer. The SAD pattern of the interface between the tool and coating is shown in Fig. 14f. The same diamond spot diffraction pattern as the tool substrate was observed, and the Pt coating layer-induced ring diffraction pattern and the OsO_4 coating layer-induced spot diffraction pattern also appeared, because the selected area contains both tool and coating layer. No evident diffraction pattern of graphite was observed [40]. Although the ring patterns induced by the amorphous coating layers will interfere with the determination of whether amorphization has occurred beneath the wear land, it can be concluded that the microstructure of the diamond tool is not changed in the subsurface more than ~80 nm away from the wear land. Moreover, from Fig. 14c, it can be seen that the wear land and the rake face formed a new cutting edge with a radius of ~5 nm. Considering

that commercial diamond tools usually have a cutting edge radius of 20–50 nm [41], it can be inferred that the cutting edge became sharper instead, owing to the formation of flank wear in the cutting of SiC, which has never been reported in cutting SiC before. Therefore, chips can be generated in ductile mode even the flank wear has occurred. However, the formation of wear land increased the contact area between the tool and the machined surface, leading to an increased friction force at tool-workpiece interfaces. As a result, the friction-induced tensile stress in the machined surface was increased, which may cause the cracks to initiate. In other words, the ductile-mode chip generation does not necessarily make machined surfaces free of cracks.

4. Discussion of cutting mechanism

Based on the observation of the surface topographies of the P-, I-, and S-dimples, two facts are clear. First, the microcracks tend to form at the feed-in/cut-in area of a dimple and propagate perpendicularly to the direction of cutting. Second, the P-dimple has the lowest resistances to surface microcracking, whereas the S-dimple has the highest.

In spherical dimple cutting, the depth of cut (d_n) varies with the position of the tool, causing a variation in undeformed chip thickness. Fig. 15 displays the schematic models of the undeformed chip cross section when the tool is at feed-in and feed-out positions. The centres of the tool for the current and next paths are at O_n and O_{n+1}. O'_{n+1} is the tool centre for the next path if d_n is constant when a flat surface is machined. Therefore, the maximum undeformed chip thickness for cutting a flat surface, h'_m, is expressed as follows:

$$h'_m = R - c \tag{1}$$

where $c = \sqrt{R^2 + f^2 - 2f\sqrt{2Rd_n - d_n^2}}$, $f = |X_{n+1} - X_n|$ is the tool feed rate, and R is the tool nose radius.

The angular position of h'_m can be written below:

$$\theta' = \cos^{-1}\frac{R - d_n}{R - h'_m} \tag{2}$$

Therefore, the distance between A (the point corresponding to the apex of the undeformed chip thickness) and O_{n+1}, as illustrated in Fig. 15, can be calculated as follows:

$$b = \begin{cases} \sqrt{c^2 + a^2 - 2ac\cdot\cos\theta'} & \text{during feed–in} \\ \sqrt{c^2 + a^2 - 2ac\cdot\cos(\pi - \theta')} & \text{during feed–out} \end{cases} \tag{3}$$

where $a = |\Delta Z| = |Z_{n+1} - Z_n|$ and is determined by f and R_d.

When $f > |\Delta Z|$, the maximum undeformed chip thickness for dimple cutting, h_m, is obtained as follows:

$$h_m = R - b \tag{4}$$

Substituting the control point cloud of dimples into equations (1)–(4), the variation in h_m with respect to the position of the tool during machining spherical dimples can be obtained.

Fig. 16a depicts the variation in h_m along the angular position $C = 0°$ while a dimple with C2E feed is cut. The value of h_m suddenly increases from zero to a high value at the feed-in stage, and then increases to a maximum before the tool feeds to the centre of the dimple. Thereafter, the h_m gradually decreases to zero as the tool feeds out. The variation in h_m is asymmetrical in the direction of the tool feed, which is consistent with the trend of the cutting forces depicted in Fig. 12e. This implies that the large undeformed chip thickness in the feed-in area causes the high cutting forces.

In contrast, h_m is symmetrical with respect to the dimple centre in the cutting direction, as depicted in Fig. 16b. Therefore, F_c is also symmetric, as proven by the experimental result presented in Fig. 12f. However, at the cut-in stage, the tool not only moves forward but also indents into the workpiece, similar to the loading process of indentation. In contrast, the tool withdraws from the workpiece at the cut-out stage, similar to the unloading process of indentation. Therefore, for the same

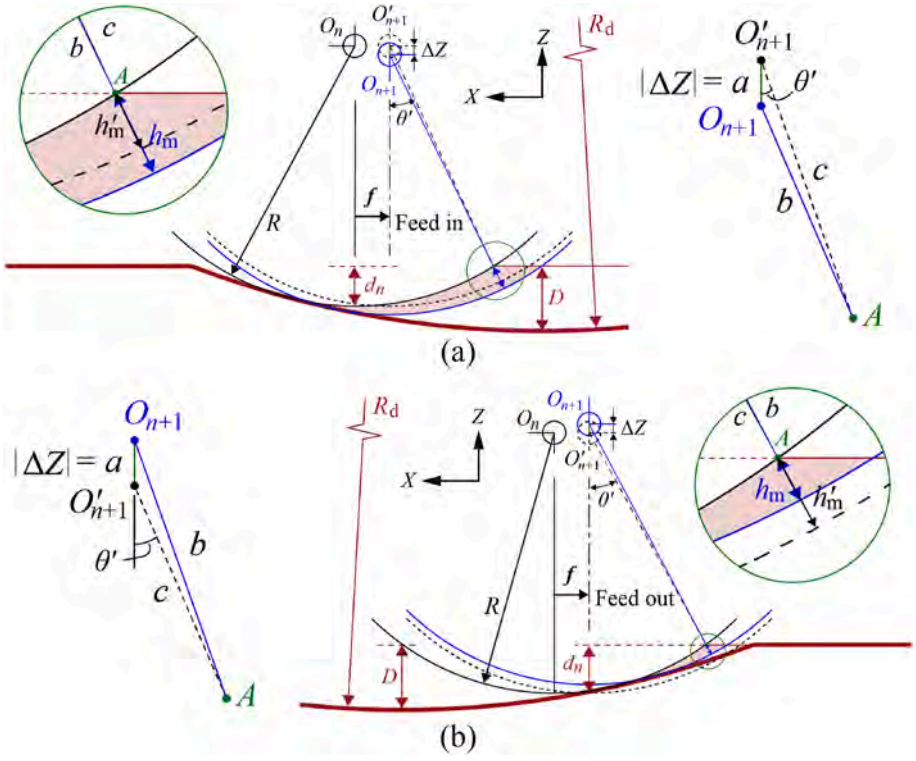

Fig. 15. Schematics of undeformed chip thickness in cutting a spherical dimple in two situations: (a) feed-in, and (b) feed-out (the region in red colour indicates the undeformed chip). (For interpretation of the references to colour in this figure legend, the reader is referred to the Web version of this article.)

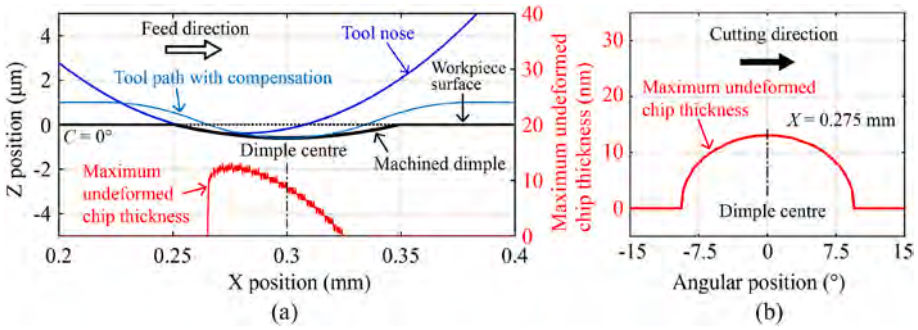

Fig. 16. Variation in maximum undeformed chip thickness: (a) along feed direction, and (b) along cutting direction.

undeformed chip thickness, the F_t is greater at the cut-in stage than at the cut-out stage, as depicted in Fig. 12f. Meanwhile, with the formation of flank wear on the tool, the tool-workpiece contact area when the tool cuts into workpiece is larger than that when the tool cuts out. Therefore, as illustrated in Fig. 17a, owing to both the larger thrust force and larger tool-workpiece contact area when the tool cuts into workpiece, a larger friction-induced tensile stress is produced in the machined surface in the cut-in area. This causes microcracks to propagate perpendicular to the machined surface, even if the chip is generated by plastic deformation in front of the tool. Moreover, as the tool moves forward the tensile stress along the shear plane due to the separation of chips from workpiece can deflect cracks. In the cut-out area, however, the friction-induced tensile stress is much smaller; thus, microcracks will not form, as depicted in Fig. 17b.

In summary, on the one hand, the larger undeformed chip thickness in the feed-in area leads to larger cutting forces; on the other hand, the larger thrust force and tool-workpiece contact area in the cut-in area cause larger tensile stress. The combination of these two factors causes microcracking at the feed-in/cut-in areas. Moreover, 4H–SiC exhibits strong anisotropy of fracture toughness for various crystal planes. For example, the theoretical fracture toughness on the {10−10} planes is 30% lower than that on the {−12−10} planes [42]. Therefore, Mode-I microcracks are easy to form along the <−12−10> directions (parallel to the {10−10} planes) within the P-dimples owing to the tensile stress in the cutting directions of <10−10>.

5. Crack-free dimple fabrication

The analysis described in Section 4 indicates that the cutting directions for less crack formation is <−12−10>. Therefore, the angular position S is optimal for fabricating crack-free dimples. In addition, a larger dimple curvature radius (R_d) and a smaller tool feed rate (f) are beneficial, as they reduce the thrust force. To demonstrate the feasibility of generating crack-free dimples in SiC, four dimples with R_d = 3 mm were fabricated one by one at the angular position S with f = 0.2 μm/rev. Two dimples were cut with E2C feed, and the other two were cut with C2E feed to distribute tool wear evenly. Fig. 18 presents a DIC microscopy image of the machined S-dimples. The sequence of the dimple machining is also indicated in the figure. Crack-free surfaces were obtained for all the dimples. The size of the machined dimples is different, because of a slight inclination between the workpiece surface and machine tool XY plane.

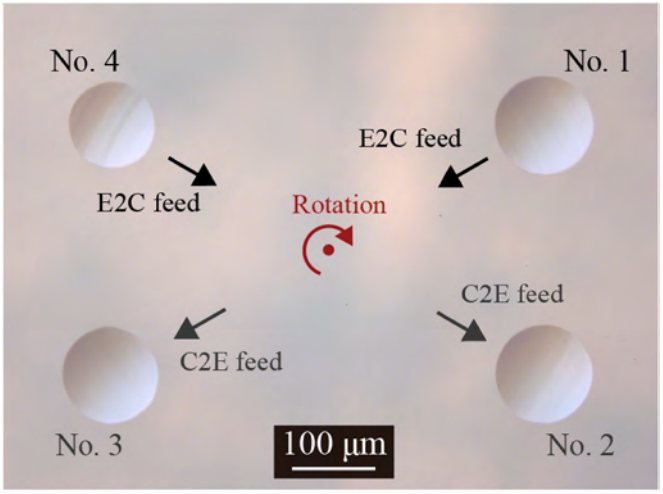

Fig. 18. DIC microscopy image of the crack-free dimples machined at the angular positions in <10−10> directions. (C2E: centre-to-edge, and E2C: edge-to-centre).

The three-dimensional topographies of the No. 1 to No.4 dimples indicated in Fig. 18 are presented in Fig. 19a1–d1, respectively. Smooth optical surfaces were obtained in all dimples. The surface roughness for No. 1 to No.4 dimples are 3.36, 4.77, 5.84, 6.30 nm Sa, respectively. There is a trend that the surface roughness becomes larger with increasing cutting distance. Besides, the edge contour of the first machined dimple (No. 1 dimple) is almost a perfect circle, while in the following machined dimples, their edge contours are gradually distorted. The edges around cut-in and cut-out areas of the dimple, especially where the tool passes through the centre of the dimple, have the most severe distortion. This is because the centre point of the cutting

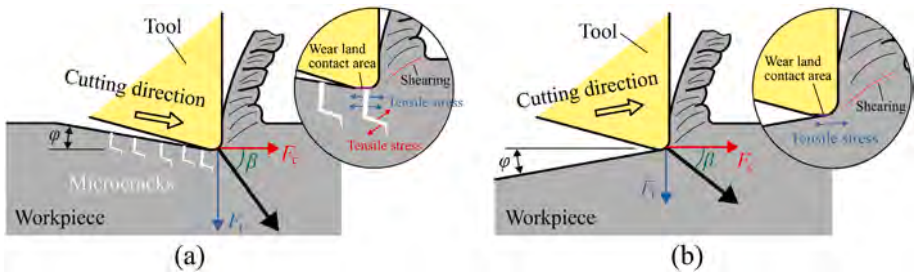

Fig. 17. Schematics of surface formation during cutting a spherical dimple: (a) the tool in the cut-in area, and (b) the tool in the cut-out area.

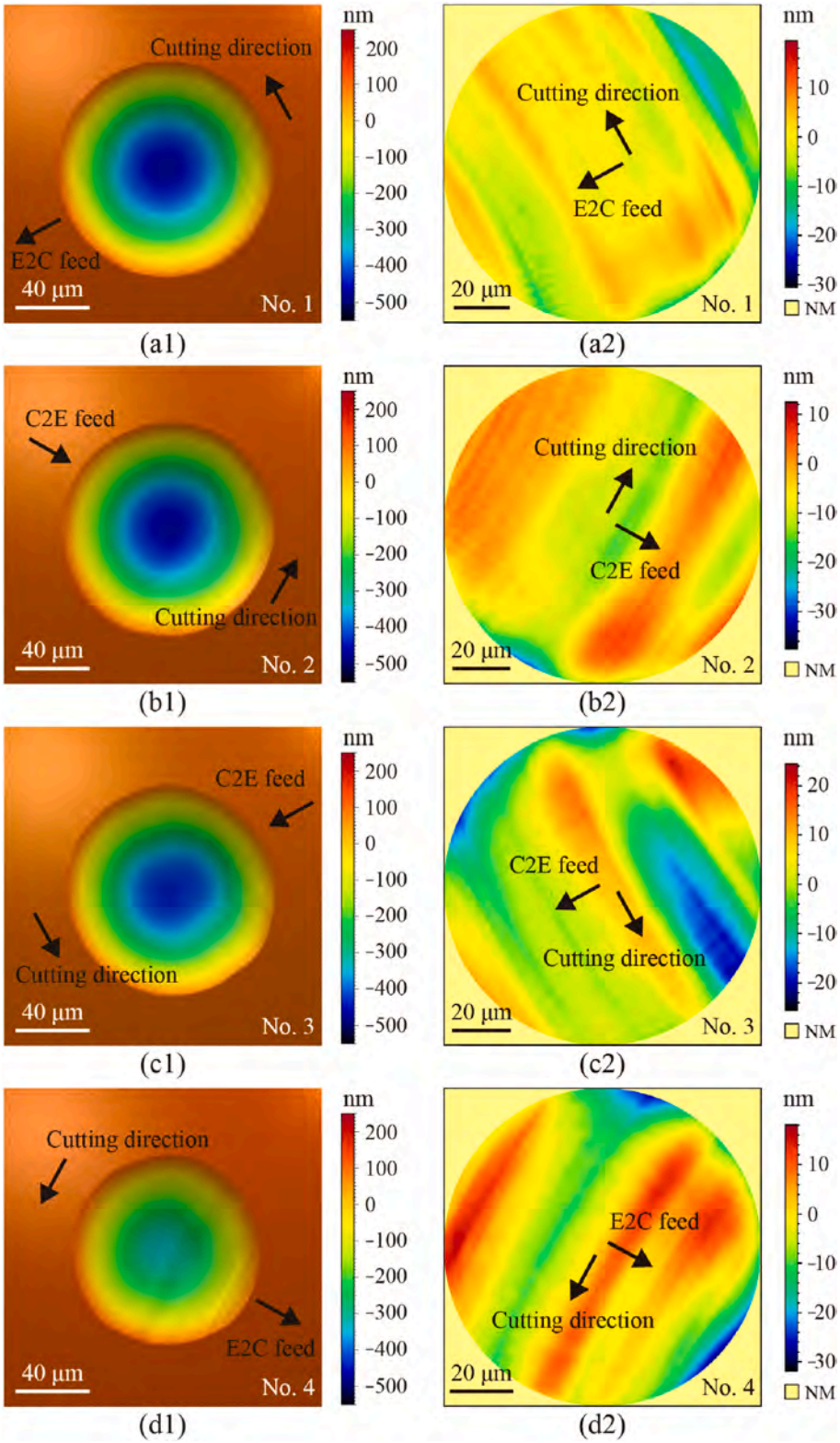

Fig. 19. (a1)–(d1) are the three-dimensional topographies of the No. 1 to No.4 dimples shown in Fig. 18; (a2)–(d2) are the form errors of the corresponding dimples. (C2E: centre-to-edge, and E2C: edge-to-centre).

edge is the most involved in the cutting process, and thus tool wear at centre point is the most severe. The form errors of the No. 1 to No.4 dimples are presented Fig. 19a2–d2. The peak to valley form error is 26.97, 35.93, 41.42, and 45.18 nm, respectively. A trend that the form error increases with increasing cutting distance can be clearly observed, which is attributed to the accumulated tool wear. It can be inferred from the demonstration experiment that diamond tools can fabricate crack-free microstructured surfaces on SiC even if tool wear has occurred. However, the surface quality and form accuracy of the surface will be reduced as the tool wear accumulates.

6. Conclusions

Micro spherical dimples were machined at various orientations of a single-crystal 4H–SiC (0001) wafer through diamond turning. The mechanisms of tool-workpiece interaction were revealed by investigating surface/subsurface damages of the machined workpieces and the used tools, as well as cutting chips and cutting forces. The feasibility of fabricating ultraprecision curved microstructured surfaces on SiC with diamond turning is demonstrated. The main conclusions are as follows:

(1) Despite continuous chips were produced, indicating ductile-mode formation of chips, surface cracks tend to form in the feed-in/cut-in areas of the dimples where higher thrust cutting forces were generated.
(2) The formation of surface cracks is mainly caused by the tensile stress along the cutting direction induced by the friction of the tool-workpiece interface, causing cracks to extend perpendicular to the machined surface. Additionally, as the tool moves forward the tensile stress along the shear plane due to the separation of chips from the workpiece deflects the cracks in the cutting direction.
(3) The optimal cutting direction for preventing crack formation is along the <−12−10> crystal orientation. However, a thick subsurface damage layer, including a disordered layer, dislocations, and stacking fault, is also formed when cutting along this direction. Cutting along <10−10> crystal orientation is likely to cause both severe surface cracks and thick subsurface damage layers. Cutting along the direction between <−12−10> and <10−10> crystal orientations allows for the generation of a shallower subsurface damage layer, but surface cracks are more likely to form.
(4) The dominant tool wear pattern was flank wear with nanoscale grooves, which is a result of continuous squeezing of the tool flank face by the tool feed marks on the machined surface. Because only flank wear occurred without edge chipping, the flank face was abraded off layer by layer and formed a new cutting edge with the rake face that was even sharper than the cutting edge before use. However, the flank wear increased the contact area of the tool, which is negative for generating high-quality surfaces. No obvious subsurface damage and graphitization were observed in the tool.
(5) Crack-free dimples with nanometric surface roughness were successfully fabricated at angular positions in <10−10> orientations by increasing the dimple curvature radius and reducing the tool feed rate. The best surface quality and form accuracy of the dimple can reach the roughness of 3.36 nm Sa and form error of 26.97 nm peak to valley, respectively.

The results of this study demonstrate that diamond turning is an effective method for producing microstructured surfaces on SiC where the choice of preferred cutting direction should be determined by the trade-off between machined surface quality and subsurface quality. The findings from this study provide guidance for the ductile machining of SiC for fabricating freeform surfaces, such as molds for replicating microlens arrays on glass. As progressive tool wear causes the deterioration of form accuracy and increase of surface roughness, efforts will be made in the future to develop techniques for the suppression of tool wear for SiC cutting.

CRediT authorship contribution statement

Weihai Huang: Writing – original draft, Visualization, Methodology, Investigation, Formal analysis, Data curation, Conceptualization. **Jiwang Yan:** Supervision, Resources, Project administration, Methodology, Funding acquisition, Conceptualization, Writing - review & editing.

Declaration of competing interest

The authors declare that they have no known competing financial interests or personal relationships that could have appeared to influence the work reported in this paper.

Data availability

Data will be made available on request.

Acknowledgments

The authors thank Mrs. Satomi Kojima, Mrs. Kawori Tanaka, and Mrs. Mayuko Tsuchiya in the Central Testing Center of Keio University for their technical assistance in SEM and TEM observations, as well as FIB sample preparations. This work has been partially supported by Japan Society for the Promotion of Science, Grant-in-Aid for Scientific Research (B), project number 21H01230.

References

[1] T. Itoh, S. Tanaka, L. Jing-Feng, R. Watanabe, M. Esashi, Silicon-carbide microfabrication by silicon lost molding for glass-press molds, J. Microelectromech. Syst. 15 (4) (2006) 859–863.
[2] A. Beaucamp, Y. Namba, H. Combrinck, P. Charlton, R. Freeman, Shape adaptive grinding of CVD silicon carbide, CIRP Annals 63 (1) (2014) 317–320.
[3] X. Yang, X. Yang, K. Kawai, K. Arima, K. Yamamura, Highly efficient planarization of sliced 4H–SiC (0001) wafer by slurryless electrochemical mechanical polishing, Int. J. Mach. Tool Manufact. 144 (2019), 103431.
[4] K. Yamamura, T. Takiguchi, M. Ueda, H. Deng, A.N. Hattori, N. Zettsu, Plasma assisted polishing of single crystal SiC for obtaining atomically flat strain-free surface, CIRP Annals 60 (1) (2011) 571–574.
[5] L. Zhang, N.J. Naples, W. Zhou, A.Y. Yi, Fabrication of infrared hexagonal microlens array by novel diamond turning method and precision glass molding, J. Micromech. Microeng. 29 (6) (2019), 065004.
[6] W. Choi, R. Shin, J. Lim, S. Kang, Design methodology for a confocal imaging system using an objective microlens array with an increased working distance, Sci. Rep. 6 (1) (2016), 33278.
[7] H. Suzuki, M. Okada, W. Asai, H. Sumiya, K. Harano, Y. Yamagata, K. Miura, Micro milling tool made of nano-polycrystalline diamond for precision cutting of SiC, CIRP Annals 66 (1) (2017) 93–96.
[8] M. Mukaida, J. Yan, Ductile machining of single-crystal silicon for microlens arrays by ultraprecision diamond turning using a slow tool servo, Int. J. Mach. Tool Manufact. 115 (2017) 2–14.
[9] Z. Sun, S. To, S. Zhang, A novel ductile machining model of single-crystal silicon for freeform surfaces with large azimuthal height variation by ultra-precision fly cutting, Int. J. Mach. Tool Manufact. 135 (2018) 1–11.
[10] J. Patten, W. Gao, K. Yasuto, Ductile regime nanomachining of single-crystal silicon carbide, J. Manuf. Sci. Eng. 127 (3) (2004) 522–532.
[11] S. Goel, X. Luo, P. Comley, R.L. Reuben, A. Cox, Brittle–ductile transition during diamond turning of single crystal silicon carbide, Int. J. Mach. Tool Manufact. 65 (2013) 15–21.
[12] J. Yan, Z. Zhang, T. Kuriyagawa, Mechanism for material removal in diamond turning of reaction-bonded silicon carbide, Int. J. Mach. Tool Manufact. 49 (5) (2009) 366–374.
[13] A. Nawaz, W.G. Mao, C. Lu, Y.G. Shen, Nano-scale elastic-plastic properties and indentation-induced deformation of single crystal 4H-SiC, J. Mech. Behav. Biomed. Mater. 66 (2017) 172–180.
[14] Z. Zhang, J. Yan, T. Kuriyagawa, Study on tool wear characteristics in diamond turning of reaction-bonded silicon carbide, Int. J. Adv. Des. Manuf. Technol. 57 (1) (2011) 117–125.
[15] K. You, G. Yan, X. Luo, M.D. Gilchrist, F. Fang, Advances in laser assisted machining of hard and brittle materials, J. Manuf. Process. 58 (2020) 677–692.
[16] J. Zhang, L. Han, J. Zhang, H. Liu, Y. Yan, T. Sun, Brittle-to-ductile transition in elliptical vibration-assisted diamond cutting of reaction-bonded silicon carbide, J. Manuf. Process. 45 (2019) 670–681.
[17] J. Yan, Z. Zhang, T. Kuriyagawa, Effect of nanoparticle lubrication in diamond turning of reaction-bonded SiC, Int. J. Autom. Technol. 5 (3) (2011) 307–312.
[18] S. Zhang, Y. Qi, J. Chen, Brittle−ductile transition behavior of 6H-SiC in oblique diamond cutting, Int. J. Mech. Sci. 246 (2023), 108155.
[19] H. Tanaka, S. Shimada, Damage-free machining of monocrystalline silicon carbide, CIRP Annals 62 (1) (2013) 55–58.
[20] Q. Kang, X. Fang, C. Wu, H. Sun, Z. Fang, B. Tian, L. Zhao, S. Wang, N. Zhu, P. Verma, M. Ryutaro, Z. Jiang, Improvement mechanism of brittle-plastic transition and residual stress in scratching 4H–SiC implanted by hydrogen ions, Ceram. Int. 48 (18) (2022) 27076–27087.
[21] J. Wang, F. Fang, Nanometric cutting mechanism of silicon carbide, CIRP Annals 70 (1) (2021) 29–32.

[22] L. Zhao, J. Zhang, J. Zhang, A. Hartmaier, T. Sun, Formation of high density stacking faults in polycrystalline 3C-SiC by vibration-assisted diamond cutting, J. Eur. Ceram. Soc. 42 (13) (2022) 5448–5457.
[23] J. Hu, Y. He, Z. Li, L. Zhang, On the deformation mechanism of SiC under nano-scratching: an experimental investigation, Wear 522 (2023), 204871.
[24] S. Gao, H. Wang, H. Huang, R. Kang, Molecular simulation of the plastic deformation and crack formation in single grit grinding of 4H-SiC single crystal, Int. J. Mech. Sci. 247 (2023), 108147.
[25] L. Zhao, W. Hu, Q. Zhang, J. Zhang, J. Zhang, T. Sun, Atomistic origin of brittle-to-ductile transition behavior of polycrystalline 3C–SiC in diamond cutting, Ceram. Int. 47 (17) (2021) 23895–23904.
[26] G. Xiao, S. To, G. Zhang, The mechanism of ductile deformation in ductile regime machining of 6H SiC, Comput. Mater. Sci. 98 (2015) 178–188.
[27] S. Zhang, X. Cheng, J. Chen, Surface deformation, phase transition and dislocation mechanisms of single crystalline 6H-SiC in oblique nano-cutting, Appl. Surf. Sci. 588 (2022), 152944.
[28] Z. Zhu, S. To, W. Zhu, P. Huang, X. Zhou, Cutting forces in fast-/slow tool servo diamond turning of micro-structured surfaces, Int. J. Mach. Tool Manufact. 136 (2019) 62–75.
[29] H. Du, M. Jiang, Z. Zhu, Z. Wang, S. To, Ultraprecision tool-servo cutting of pure nickel for fabricating micro/nanostructure arrays, Mater. Des. 221 (2022), 110913.
[30] S. Goel, X. Luo, R.L. Reuben, W.B. Rashid, Atomistic aspects of ductile responses of cubic silicon carbide during nanometric cutting, Nanoscale Res. Lett. 6 (1) (2011) 589.
[31] S. Goel, X. Luo, R.L. Reuben, Molecular dynamics simulation model for the quantitative assessment of tool wear during single point diamond turning of cubic silicon carbide, Comput. Mater. Sci. 51 (1) (2012) 402–408.
[32] X. Luo, S. Goel, R.L. Reuben, A quantitative assessment of nanometric machinability of major polytypes of single crystal silicon carbide, J. Eur. Ceram. Soc. 32 (12) (2012) 3423–3434.
[33] National Center for Biotechnology Information, PubChem Compound Summary for CID 30318, Osmium tetroxide, 2023. https://pubchem.ncbi.nlm.nih.gov/compound/Osmium-tetroxide (accessed May 14th 2023).
[34] M. Schroeder, Osmium tetraoxide cis hydroxylation of unsaturated substrates, Chem. Rev. 80 (2) (1980) 187–213.
[35] M. Matsumoto, H. Huang, H. Harada, K. Kakimoto, J. Yan, On the phase transformation of single-crystal 4H–SiC during nanoindentation, J. Phys. Appl. Phys. 50 (26) (2017), 265303.
[36] J. Li, G. Yang, X. Liu, H. Luo, L. Xu, Y. Zhang, C. Cui, X. Pi, D. Yang, R. Wang, Dislocations in 4H silicon carbide, J. Phys. Appl. Phys. 55 (46) (2022), 463001.
[37] J. Demenet, M. Amer, C. Tromas, D. Eyidi, J. Rabier, Dislocations in 4H- and 3C-SiC single crystals in the brittle regime, Phys. Status Solidi C 10 (1) (2013) 64–67.
[38] S. Nakashima, M. Higashihira, K. Maeda, H. Tanaka, Raman scattering characterization of polytype in silicon carbide ceramics: comparison with X-ray diffraction, J. Am. Ceram. Soc. 86 (5) (2003) 823–829.
[39] D.P. Yu, S.W. Gan, Y.S. Wong, G.S. Hong, M. Rahman, J. Yao, Optimized tool path generation for fast tool servo diamond turning of micro-structured surfaces, Int. J. Adv. Des. Manuf. Technol. 63 (9) (2012) 1137–1152.
[40] V. Datsyuk, S. Trotsenko, S. Reich, In situ thermal polymerisation of natural oils as novel sustainable approach in nanographite particle production, Appl. Phys. A 124 (1) (2017) 30.
[41] W. Huang, J. Yan, Effect of tool geometry on ultraprecision machining of soft-brittle materials: a comprehensive review, Int. J. Extrem. Manuf. 5 (1) (2023), 012003.
[42] C. Kunka, A. Trachet, G. Subhash, Interaction of indentation-induced cracks on single-crystal silicon carbide, J. Am. Ceram. Soc. 98 (6) (2015) 1891–1897.